RSC Advances

PAPER

View Article Online
View Journal | View Issue

Cite this: *RSC Adv.*, 2025, **15**, 27016

Design of a simple solution-processed universal shell for synthesizing reverse type-I core–shell structures toward high-efficiency water-splitting photocathodes†

Minju Kim,‡[a] Jeong-Mi Yeon,‡[cd] G. Hwan Park,[e] Hyunjung Kim,[f] Minseo Kim,[e] Sun Yong Choi,[c] Sung Won Hwang,*[g] Sung-Hwan Lim*[d] and Hanleem Lee*[ab]

Core–shell colloidal nanocrystals (CNCs) are promising candidates for photoelectrochemical (PEC) photocathodes due to their strong light absorption, tunable bandgaps, and efficient charge separation. In this study, we developed a simple and versatile strategy for fabricating narrow-bandgap shells compatible with various core materials. Among the configurations tested, the matrix-type MoS_x shell demonstrated the most effective performance, significantly enhancing photocurrent generation and operational stability through improved surface defect passivation and charge carrier separation. Band-level engineering further enabled the formation of reverse type-I heterojunctions in both CdSe and CIS_2 CNCs. Although type-II systems are traditionally favored for charge separation, our results show that the reverse type-I architecture not only enhances photocarrier separation under standard illumination but also effectively suppresses dark current. This is attributed to the dual physical and electronic passivation provided by the reverse type-I structure, which stabilizes the core–shell interface and reduces nonradiative recombination. Notably, the Cu_2O/CuO/red CIS_2 CNCs with a high indium ratio achieved the highest photocurrent density and retained over 86% of their initial performance after 24 hours of continuous operation at −0.1 V *vs.* RHE, demonstrating excellent long-term stability. These results highlight the strong potential of matrix-type reverse type-I core–shell CNCs as efficient and durable photocathode materials for PEC applications.

Received 15th June 2025
Accepted 24th July 2025

DOI: 10.1039/d5ra04253d

rsc.li/rsc-advances

Introduction

Amid growing global demand for environmentally friendly and sustainable energy sources, green hydrogen production technologies—characterized by zero carbon emissions during the production process—have garnered significant attention. Among these, water splitting driven by electricity generated from renewable sources such as solar and wind energy is emerging as a key component of power-to-gas systems. In particular, photoelectrochemical (PEC) water splitting, which enables the direct utilization of solar energy for hydrogen generation, is recognized as a promising green hydrogen production technology based on energy harvesting. PEC-based water splitting systems are broadly classified into two main approaches: those employing photovoltaic cells and those utilizing photoelectrodes.[1] The photoelectrode-based approach offers advantages such as a simpler structure, ease of fabrication, and lower production costs. However, it suffers from lower performance compared to systems that utilize photovoltaic cells. To overcome this limitation, it is essential to develop novel photoelectrode materials that facilitate efficient photocarrier generation and transport while ensuring high stability.[2]

Photoelectrode materials for PEC catalysts must simultaneously exhibit efficient photocarrier generation and strong catalytic activity, making their design inherently more complex than that of conventional electrocatalysts. Colloidal

[a]*Department of Chemistry, Myongji University, 116 Myongji Ro, Yongin, Gyeonggi-do, 17058, South Korea. E-mail: hanleem@mju.ac.kr*

[b]*Division of Chemistry and Energy Convergence, College of Chemistry and Life Sciences, Myongji University, 116 Myongji Ro, Yongin, Gyeonggi-do, 17058, South Korea*

[c]*Nano Materials R&BD Division, Cheorwon Plasma Research Institute, 4620, Hoguk-ro, Galmal-eup, Cheorwon-gun, Gangwon-do, Republic of Korea*

[d]*Department of Advanced Materials Science & Engineering, Kangwon National University, Chuncheon-si, 24341, Republic of Korea*

[e]*Department of Chemistry, Sungkyunkwan University (SKKU), Suwon 16419, Republic of Korea*

[f]*Research Institute of Basic Sciences, Sungkyunkwan University (SKKU), Suwon 16419, Republic of Korea*

[g]*Department of System Semiconductor Engineering, Sangmyung University, 31 Sangmyeongdae-gil, Dongnam-gu, Cheonan 31066, Chungcheongnam-do, Republic of Korea*

† Electronic supplementary information (ESI) available. See DOI: https://doi.org/10.1039/d5ra04253d

‡ The authors contributed to the manuscript equally.

nanocrystals (CNCs) have attracted considerable attention as promising candidates for photoelectrodes due to their tunable electrical and optical properties.[3] In particular, core–shell structured CNCs are of great interest for their multifunctionality:[4,5] photocarrier generation and light absorption can be tuned *via* the core, while catalytic activity can be optimized by engineering the shell composition. Various types of core–shell CNCs have been investigated for PEC applications for both photocathode and photoanode. These include lead chalcogenides (PbX, where X = S, Se, or Te), cadmium chalcogenides (CdX, where X = S, Se, or Te),[6] and less toxic alternatives such as copper indium chalcogenides (CIX_2). For example, Lu *et al.* demonstrated a PEC photocathode comprising p-type NiO coupled with ZnSe/CdS and CdS/ZnSe quantum dots. The system achieved cathodic photocurrent densities of 57 μA cm^{-2} for ZnSe/CdS and 49 μA cm^{-2} for CdS/ZnSe at 0 V *vs.* RHE during photoelectrochemical water reduction.[7] In general, most CNC-based PEC photocathodes without noble metal co-catalysts have exhibited cathodic photocurrents in the microampere (μA) range. These values remain significantly lower than those achieved by wide-bandgap metal oxide systems,[8,9] despite the inherently superior exciton generation efficiency and higher extinction coefficients of narrow-bandgap CNCs—properties closely linked to enhanced photocarrier generation.[10]

The limited performance of CNCs is primarily attributed to inadequate charge separation, high moisture sensitivity, and poor long-term stability, which are largely caused by surface defect.[11] Furthermore, most existing core–shell strategies have adopted type-I architectures due to constraints in shell material selection imposed by lattice strain. Type-I core–shell structures, which typically employ wide-bandgap shells, provide excellent surface passivation through the formation of a potential energy well. However, while this configuration enhances structural stability, it often impedes efficient charge carrier separation. Additionally, many wide-bandgap shell materials lack intrinsic catalytic activity, further limiting their effectiveness in PEC applications, particularly in the absence of noble metal co-catalysts.[12] Therefore, there is a critical need to develop novel core–shell architectures that deliver multifunctionality—simultaneously enabling effective surface passivation, efficient charge separation, and strong catalytic activity within the shell material.

In this study, a simple solution-processed reverse type-I core–shell structure was developed as an effective photoelectrode for PEC applications. The reverse type-I architecture was selected due to its ability to facilitate efficient charge extraction and enhance charge injection rate.[13] Copper indium sulfide (CIS_2) or copper indium selenide ($CISe_2$) CNCs were employed as the core materials, while molybdenum disulfide (MoS_x) was utilized as the shell material. To mitigate lattice strain, a composite MoS_x shell comprising both amorphous and crystalline phases was introduced. Then, band alignment of the CIX_2@MoS_x core–shell structures was precisely tuned by adjusting the In/Cu ratio in the core and modulating the amorphous-to-crystalline ratio in the shell. The PEC performance of each material configuration was systematically investigated to evaluate the effects of shell characteristics (*i.e.*, phase composition and band alignment) on photocarrier generation, charge separation, and device stability.

Result and discussion

In our previous study, we examined photocarrier generation and extraction behavior as a function of shell characteristics using impedance analysis.[14] Four types of ligands were employed as shell components: insulating ligands, organic molecular linkers, inorganic molecular linkers, and matrix-type ligands. Among these, the matrix-type ligand system exhibited a pronounced enhancement in photocarrier separation efficiency. This improvement was attributed to the presence of multiple charge separation pathways—enabled by enhanced carrier transport through sub-bandgap states facilitated by amorphous MoS_x—and the effective passivation of trap states in the CNCs, which collectively contributed to the reduction of Fermi-level pinning. As a result, the matrix-type core–shell system effectively suppressed hot carrier-induced trap state formation, minimized photoinduced recombination, and improved operational stability—particularly in narrow-bandgap photodetector applications. Building on our previous findings, this study investigates whether the photocarrier separation behavior observed in solid-state devices remains consistent in PEC systems. From the four ligand systems previously evaluated, three representative types were selected for further analysis: insulating ligands, organic molecular linkers, and matrix-type ligands. Each represents a different core–shell configuration. The insulating ligand system serves as a model for a wide-barrier type-I core–shell structure, while the organic linker system, based on 3-mercaptopropionic acid (MPA), represents a narrow-barrier type-I configuration (Fig. 1a). In contrast, the matrix-type ligand system corresponds to a type-II core–shell structure when $CISe_2$ CNCs, possessing a near-infrared (NIR) bandgap, are used as the core material. The matrix-type ligand used in this study was synthesized *via* a previously established two-step ligand exchange method:[14] initially, $CISe_2$ CNCs underwent MPA treatment *via* a solution-phase process, followed by a solid-state ligand exchange with MoS_4^{2-} to form the final hybrid ligand shell. After the two-step ligand exchange, the size and crystallinity of the $CISe_2$ CNCs were well preserved, as confirmed by transmission electron microscopy (TEM) analysis (Fig. S1†). The final shell structure for the $CISe_2$ CNCs with the matrix-type shell was completed through thermal annealing under a nitrogen atmosphere.

First, the performance of PEC water reduction was evaluated using Cu_2O/CuO photocathodes, both with and without $CISe_2$ core–shell CNCs. As shown in Fig. 1b, the bare Cu_2O/CuO electrode exhibited a cathodic photocurrent density with a maximum difference between dark and illuminated current densities ($\Delta j = j_{light} - j_{dark}$) of approximately 2.4 mA cm^{-2} at 0.096 V *vs.* RHE under 1 sun illumination. This relatively high photocurrent density is attributed to the favorable alignment of the Cu_2O/CuO conduction band edge with the hydrogen evolution reaction (HER) potential.[15] However, the intrinsic instability of Cu_2O/CuO—primarily resulting from the reduction of copper ions—significantly limits its operational

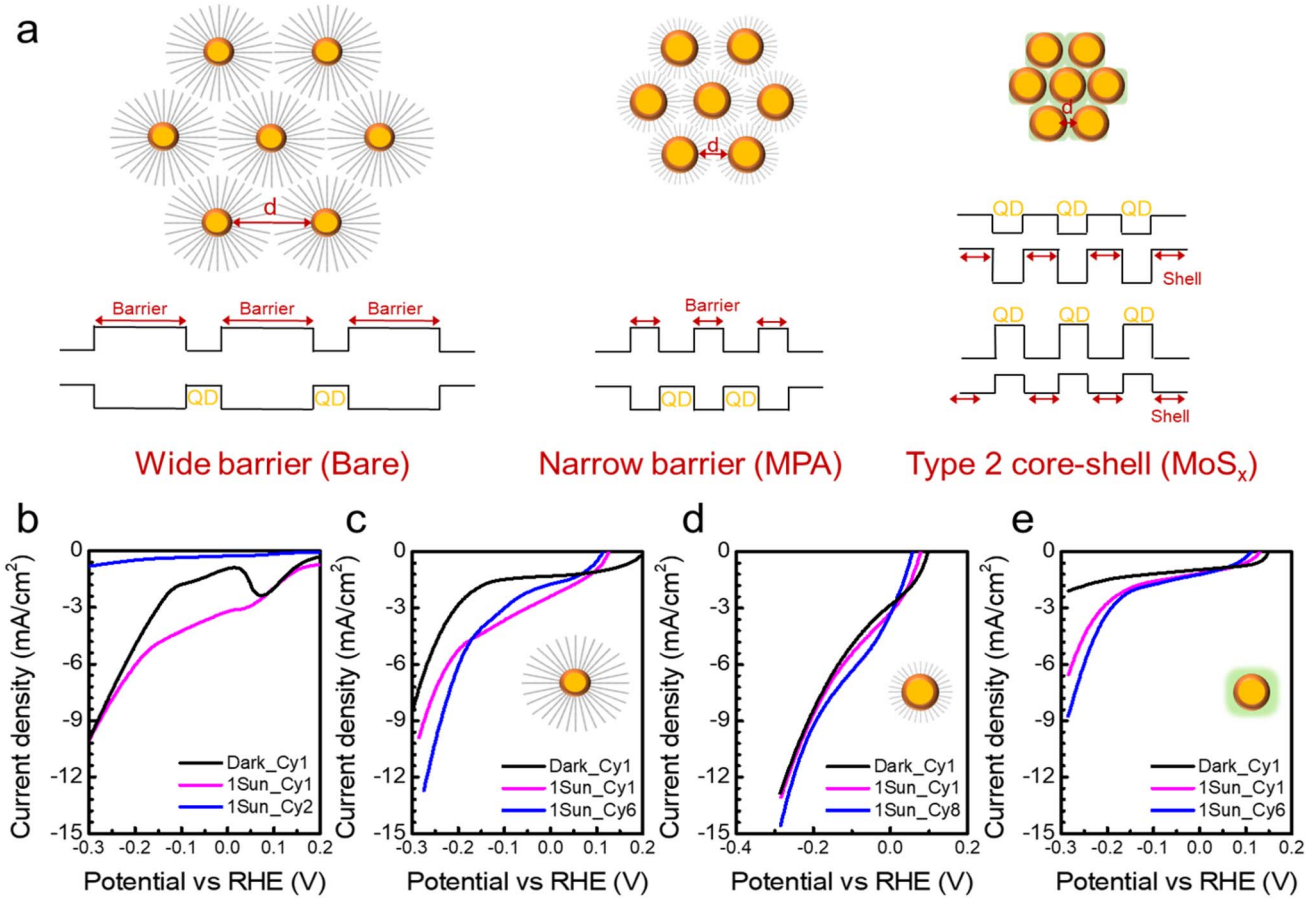

Fig. 1 (a) Schematic illustration of the band alignment of $CISe_2$ CNCs with different shell systems. (b–e) Current density *versus* cathodic potential (*J*–*V*) curves for (b) bare Cu_2O/CuO, (c) Cu_2O/CuO/$CISe_2$ CNCs capped with insulating ligands, (d) Cu_2O/CuO/$CISe_2$ CNCs capped with organic linker ligands, and (e) Cu_2O/CuO/$CISe_2$ CNCs capped with matrix-type ligands (post-annealing at 250 °C).

durability. In our measurements, a pronounced reduction peak was observed at 0.07 V *vs.* RHE, corresponding to the onset of Cu^+ reduction. As a result, the unprotected Cu_2O/CuO electrode, lacking a passivation layer, underwent simultaneous film delamination when subjected to highly negative potentials—approximately 0.07 V for the Cu^+ to Cu^0 transition, and more negative than −0.3 V for the Cu^{2+} to Cu^0 and Cu^{2+} to Cu^+ reductions. Consequently, a sharp decline in photocurrent density was observed during the second measurement cycle, indicating significant degradation of the photoelectrode (Fig. 1b).[16]

On the other hand, the PEC performance became significantly more stable after the deposition of the $CISe_2$ CNC layer on Cu_2O/CuO (Fig. 1c and d). Unlike the bare Cu_2O/CuO electrode, the $CISe_2$ CNC-modified electrodes—regardless of the ligand type—maintained high photocurrent densities even after six cycles under 1 sun illumination. However, their dark current behaviors varied noticeably depending on the ligand system. The $CISe_2$ CNCs with insulating ligands exhibited both dark and photocurrent density levels comparable to those of the bare Cu_2O/CuO, with a slight improvement in operational stability (Fig. 1c), suggesting that the CNC layer primarily functioned as a passive overlayer without significantly altering charge transport. The oleylamine ligands used have an alkyl chain length of about 1.9 nm, which is not long enough to completely block quantum tunneling. Therefore, electronic coupling within the NIR CNCs remained effective, enabling efficient separation of photogenerated electron–hole pairs even in the presence of these insulating ligands. In contrast, the $CISe_2$ CNCs with MPA ligands showed a markedly increased dark current density (Fig. 1d), attributed to enhanced electronic coupling between CNCs, which facilitated charge transport but also elevated the baseline conductivity. Meanwhile, the matrix-type shell resulted in a reduced dark current density (Fig. 1e), likely due to its superior surface defect passivation, which effectively suppressed recombination and improved operational stability—consistent with our previous observations in solid-state devices.[14]

Interestingly, photocurrent density values measured at −0.2 V *vs.* RHE (j_{light}) followed the trend: $CISe_2$ CNCs with MPA (−10.4 mA cm^{-2}) > insulating ligand (−5.8 mA cm^{-2}) > matrix-type ligand (−4.9 mA cm^{-2}). However, the matrix-type system exhibited the highest maximum Δj ($j_{light} - j_{dark}$), indicating that its PEC enhancement was primarily attributed to improved photocarrier separation rather than increased baseline conductivity. Owing to the effectively suppressed recombination

behavior enabled by the matrix-type shell, $CISe_2$ CNCs demonstrated a stable and sustained photocurrent density under continuous illumination (Fig. S2†). In contrast, the other systems exhibited progressively decreasing photocurrent density over time. Therefore, $CISe_2$ CNCs with matrix-type ligands function as both an effective passivation layer and an efficient photocarrier transport medium, positioning them as a highly promising candidate for photocathode integration in PEC applications.

The broad applicability of the matrix-type MoS_x shell was systematically investigated. Unlike conventional crystalline shell formation methods, which rely on direct shell growth immediately following core CNC synthesis, our approach utilizes a ligand exchange reaction followed by a post-annealing process to convert the initially amorphous shell into a crystalline phase. The coexistence of amorphous and crystalline MoS_x domains effectively alleviates lattice strain caused by core–shell lattice mismatch. This structural adaptability enables the matrix-type MoS_x shell to accommodate a broad range of core materials. To demonstrate the versatility of this strategy, two distinct core nanocrystal systems—CdSe and $CISe_2$ CNCs—were selected and evaluated. Fig. S3† presents TEM images of CdSe CNCs before and after ligand exchange. Consistent with the results observed for $CISe_2$ CNCs, the particle size remained largely unchanged, and the crystallinity was well preserved throughout the ligand exchange process. Zeta potential measurements showed a significant shift from −8 mV to −62 mV after ligand exchange, attributed to the negatively charged nature of the MoS_4^{2-} ligands (Fig. 2a). Additionally, FT-IR spectroscopy revealed the disappearance of characteristic CH_3 and –CH_2– stretching modes associated with insulating ligand (*i.e.*, oleylamine), further confirming the successful replacement with MoS_4^{2-} ligands on the surface of the CdSe CNCs (Fig. 2b).

The PEC water reduction performance of CdSe CNCs was evaluated, as shown in Fig. 2c. The bare CdSe CNCs exhibited a dark current density of 0.47 μA cm^{-2} and a photocurrent density of 2.0 μA cm^{-2} at −0.2 V *vs.* RHE. After ligand exchange with MoS_4^{2-}, both dark current density (2.5 μA cm^{-2} at −0.2 V) and photocurrent density (8.9 μA cm^{-2} at −0.2 V) slightly increased, attributed to enhanced conductivity. Subsequent post-annealing—intended to form a matrix-type core–shell structure similar to that developed for $CISe_2$ CNCs—led to a marked improvement in PEC performance. After annealing at 300 °C, the dark current density reached 9.0 μA cm^{-2} at −0.2 V and the photocurrent density increased to 25.2 μA cm^{-2} at −0.2 V, representing a fourfold enhancement in maximum Δj compared to the unannealed sample. Annealing at 500 °C further improved the performance, yielding a dark current density of 0.188 mA cm^{-2} at −0.2 V and a photocurrent density of 0.256 mA cm^{-2} at −0.2 V—equivalent to a 16-fold enhancement in maximum Δj. These improvements mirror the trend observed in $CISe_2$ CNCs with matrix-type shells, suggesting that our shell system can be broadly applied to various types of CNCs as effective PEC photocathode hosts.

Interestingly, as the annealing temperature increased, the maximum Δj value increased proportionally (Fig. 2c and S4a†). Ammonium tetrathiomolybdate [$(NH_4)_2MoS_4$] undergoes

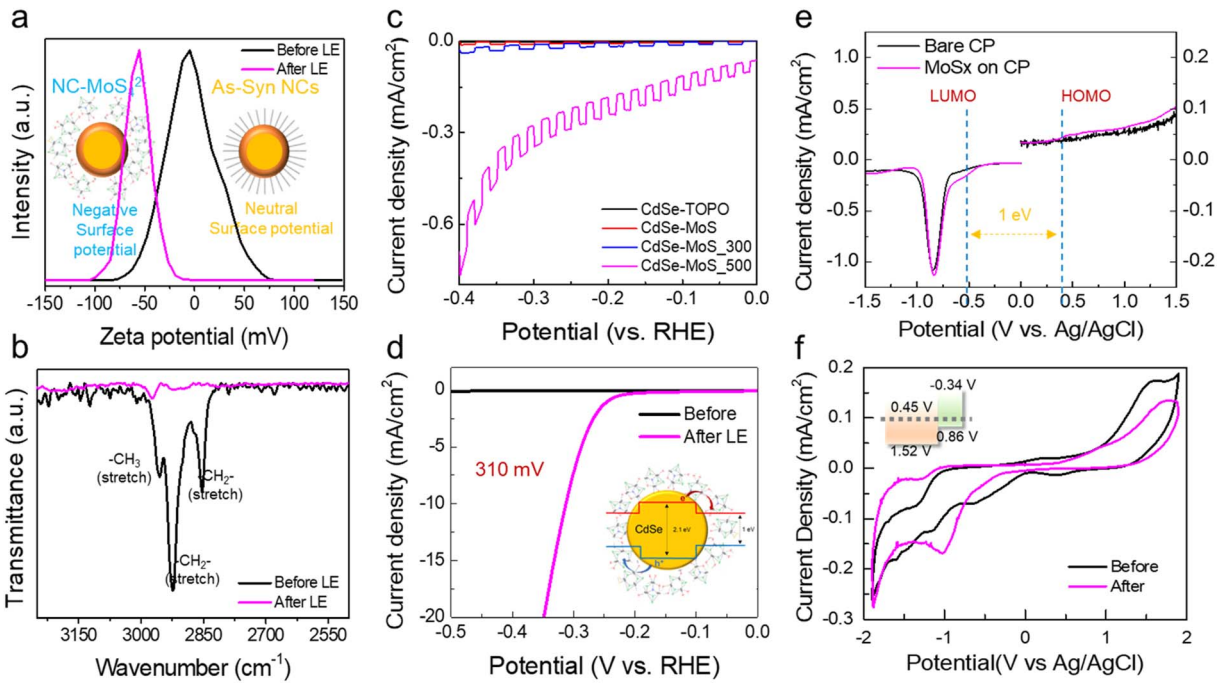

Fig. 2 (a) Zeta potential measurements of CdSe CNCs before and after MoS_4^{2-} ligand exchange. (b) FT-IR spectra of CdSe CNCs before and after MoS_4^{2-} ligand exchange. (c) *J*–*V* curves of CdSe CNC photocathodes with different ligand systems under pH 6 conditions. (d) *J*–*V* curves of bare CdSe CNCs and CdSe@MoS_x CNCs deposited on a carbon rod working electrode under pH 1 conditions. (e) Differential pulse voltammetry of bare CdSe CNCs and CdSe@MoS_x CNCs. (f) Cyclic voltammetry of $CISe_2$ CNCs and $CISe_2$@MoS_x CNCs under 0.1 M $TBAPF_6$ in acetonitrile.

thermal decomposition through the reaction: $(NH_4)_2MoS_4 \rightarrow MoS_x + 2NH_3 + H_2S$. This transformation yields a range of MoS_4^{2-}-derived phases, including crystalline MoS_2 (trigonal or hexagonal), crystalline sulfur-deficient MoS_x ($x < 2$), and sulfur-rich amorphous MoS_x, depending on the annealing conditions.[17,18] Under low-temperature annealing (<160 °C), the MoS_x shell predominantly retains its amorphous nature. At moderate temperatures (<500 °C), a phase transition from amorphous MoS_x to the 1T/1T′ MoS_x phase occurs. At higher annealing temperatures (>550 °C), the 1T phase transforms into the semiconducting 2H phase.[19] Since the 2H phase exhibits lower electrical conductivity, its formation leads to reduced photocathode performance. To avoid this and maintain high PEC activity, the annealing temperature was carefully controlled within the 160–500 °C range. It is considered that the PEC performance of CdSe@MoS_x CNCs annealed at 500 °C is primarily due to the presence of the 1T/1T′ MoS_x phase. To validate this, the *J–V* characteristics of the CdSe@MoS_x CNCs annealed at 500 °C were measured in 0.5 M H_2SO_4 electrolyte (Fig. 2d). The sample exhibited an overpotential of 310 mV, which is similar values reported for 1T/1T′ MoS_x phases,[20] further supporting our interpretation.

To better understand the role of the shell phase, the conduction band minimum (CBM) and valence band maximum (VBM) of CdSe@MoS_x CNCs were estimated using differential pulse voltammetry (DPV) as a function of annealing temperature (Fig. S5†). While annealing influenced the electronic structure, the overall bandgap of the CdSe@MoS_x CNCs remained unchanged. According to the DPV results, both the CBM and VBM exhibited slight shifts with increasing annealing temperature. Compared to bare CdSe CNCs, the CdSe@MoS_x CNC samples showed an upshift in CBM and a downshift in VBM following MoS_x shell formation (Fig. 2e). Given that the core CdSe CNCs exhibited a bandgap of approximately 2.1 eV (Fig. S6†), all three CdSe@MoS_x CNC samples—regardless of annealing temperature—maintained a reverse type-I core–shell band alignment. Therefore, the differences observed in PEC activity among these samples with varying shell characteristics are primarily attributed to enhanced electrical conductivity, rather than differences in photocarrier separation efficiency induced by band alignment at the core–shell interface.

$CISe_2$@MoS_x CNCs exhibited a similar trend. Due to the more complex sub-band structure of NIR $CISe_2$ CNCs compared to red CdSe CNCs, their band states were evaluated using cyclic voltammetry (CV) with an 0.1 M $TBAPF_6$ in acetonitrile, as shown in Fig. 2f. To ensure accurate determination of electronic energy levels, CV measurements were conducted at various scan rates (Fig. S7†). As the faradaic current is influenced by scan rate, both anodic and cathodic currents—corresponding to the VBM and CBM, respectively—are expected to increase proportionally with scan rate.[21] The potential region from approximately 0 to −0.6 V is associated with the CBM, while the region from 0 to +1 V corresponds to the VBM. The VBM position was estimated using the oxidation peak (V_{ox} *vs.* Ag/AgCl), calculated as 4.75 eV + V_{ox}, while the CBM level was determined using the reduction peak (V_{red}), calculated as 4.75 eV + V_{red}.[22] For the bare $CISe_2$ CNCs, the CBM was identified at 0.48 V and the VBM at 1.52 V (Fig. S7a and c†), indicating a bandgap of approximately 1.1 eV. In contrast, $CISe_2$@MoS_x CNCs showed a CBM around −0.34 V and a VBM around +0.86 V (Fig. S7b and c†). Based on these results, $CISe_2$@MoS_x CNCs exhibited a type-II core–shell band alignment, as illustrated in the inset of Fig. 2f.

As CIS_2 or $CISe_2$ CNCs are considered non-toxic alternatives to CdSe-based CNCs, various types of core–shell CIX_2 CNCs were investigated to examine the distinct effects of reverse type I and type II band alignment configurations on PEC performance. All core–shell CNCs were deposited onto Cu_2O/CuO photoelectrodes. Top-view SEM images (Fig. S8†) confirmed uniform and complete surface coverage of the Cu_2O/CuO substrates by the $CISe_2$@MoS_x layer. X-ray diffraction (XRD) patterns (Fig. S9†) of $CISe_2$@MoS_x-passivated Cu_2O/CuO electrodes before annealing revealed a new diffraction peak at 44.62°, corresponding to the (220) plane of $CISe_2$ nanocrystals. This observation is consistent with the FFT patterns obtained from TEM analysis (Fig. S1†). After annealing, additional peaks at 18.08° and 31.58° emerged, which are attributed to the (004) and (100) planes of the 1T/1T′ phase of MoS_x, respectively. Notably, these peaks were absent prior to annealing, indicating that the 1T/1T′ phase of MoS_x was formed during the thermal treatment. Collectively, these results confirm the successful co-deposition of $CISe_2$ and MoS_x onto the Cu_2O/CuO electrode surface and validate the effectiveness of the applied surface modification strategy in enhancing PEC activity.

To clarify the influence of the core–shell interface on PEC performance, core–shell CIX_2 CNCs were first evaluated under MPA-rich and MPA-deficient conditions. A two-step ligand exchange process involving MPA and MoS_4^{2-} led to variations in shell composition, governed by the residual surface ligand densities. Accordingly, MPA-rich CIS_2@MoS_x and MPA-deficient $CISe_2$@MoS_x CNCs were synthesized, and their PEC performances were systematically compared to assess the impact of MPA content at the interface. The MPA-rich CIS_2@MoS_x CNCs were prepared using a previously reported water-based synthesis method (see ESI†),[23] wherein MPA was introduced during the reaction. This approach eliminated the need for a separate ligand exchange step, resulting in a high surface coverage of MPA and promoting strong ion–dipole interactions that facilitated the retention of a larger amount of MoS_4^{2-} on the CNC surface. The MPA-rich CIS_2@MoS_x CNCs demonstrated a high dark current density (−10.7 mA cm^{-2} at −0.3 V *vs.* RHE), indicative of enhanced baseline conductivity due to strong electronic coupling between particles (Fig. 3a). However, a gradual decline in photocurrent was observed during prolonged operation. This degradation is attributed to the higher density of surface defects inherent to the water-based synthetic conditions, which likely facilitated hot carrier generation under illumination.[24] These hot carriers may have accelerated defect propagation at the interface, ultimately contributing to the observed performance deterioration.

In contrast, the MPA-deficient $CISe_2$@MoS_x CNCs were synthesized *via* a modified hot-injection method,[25] using dodecanethiol (DDT) as both a co-surface ligand and sulfur source. These were compared to bare $CISe_2$@MoS_x CNCs, which were also synthesized using the hot-injection method but

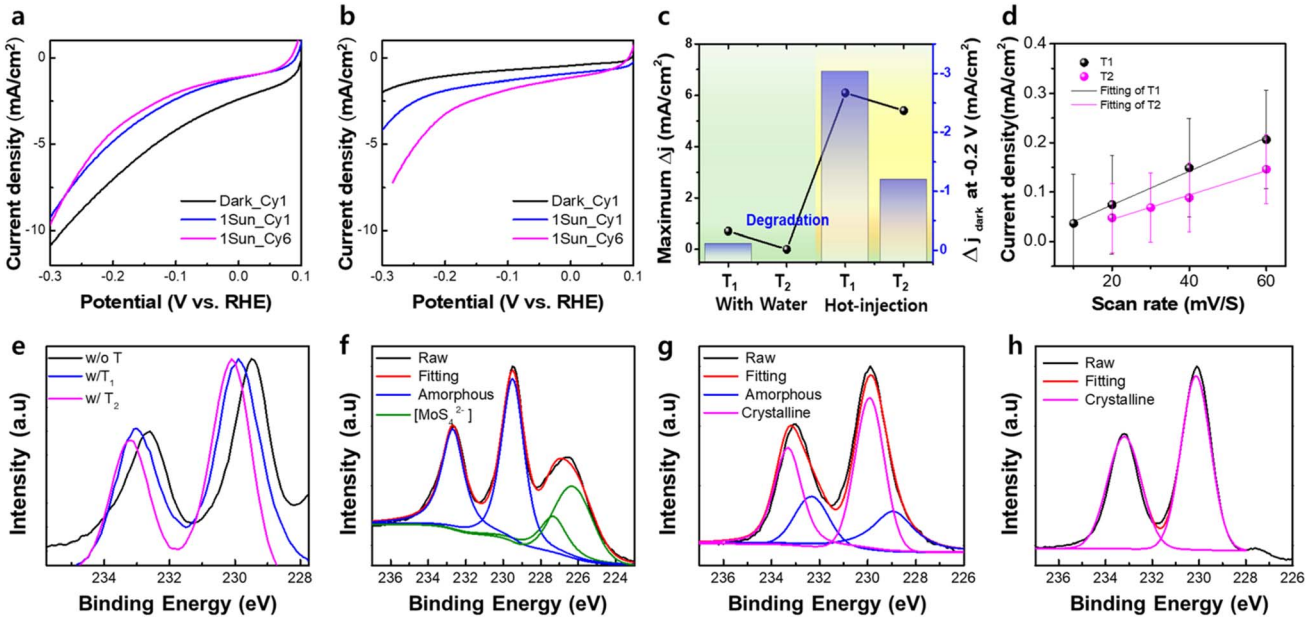

Fig. 3 (a and b) *J–V* curves of CNC photocathodes (Cu_2O/CuO/CNC layer) synthesized *via* (a) a water-based method and (b) a hot injection method. (c) Comparison of maximum Δj and dark current density changes at −0.2 V as a function of synthesis method and annealing condition. (d) ECSA estimation of $CISe_2$@MoS_x CNCs subjected to different annealing conditions. (e) XPS spectra of Mo 3d orbitals for $CISe_2$@MoS_x CNCs under different annealing conditions: without post-annealing, T_1 treatment, and T_2 treatment. (f–h) Deconvoluted XPS spectra of Mo 3d orbitals for $CISe_2$@MoS_x CNCs under each annealing condition: (f) without post-annealing, (g) T_1 treatment, and (h) T_2 treatment.

without DDT. For both types, the original insulating ligands (*e.g.*, oleylamine, DDT) were partially replaced by MPA through ligand exchange using a mild KOH solution (0.12 M in methanol). While this approach was chosen to minimize the formation of surface defects typically caused by harsher stripping conditions, it did not completely remove the insulating ligands, resulting in lower MPA surface coverage and, consequently, reduced MoS_4^{2-} binding. The MPA-deficient $CISe_2$@MoS_x CNCs exhibited a lower surface MPA content compared to the bare $CISe_2$@MoS_x CNCs, primarily because DDT ligands require significantly higher energy for removal than oleylamine. As a result, the MPA-deficient $CISe_2$@MoS_x CNCs showed a slightly reduced photocurrent density (-7.22 mA cm^{-2} at -0.3 V *vs.* RHE in Fig. 3b), which is attributed to the lower conductivity of the MPA-deficient shell relative to that of the bare $CISe_2$@MoS_x CNCs. However, the dark current densities of both samples were comparable, suggesting that the matrix-type MoS_x shell in the MPA-deficient $CISe_2$@MoS_x CNCs still effectively passivates surface defects. Interestingly, MPA-deficient $CISe_2$@MoS_x CNCs exhibited pronounced activation behavior over repeated operating cycles compared to bare $CISe_2$@MoS_x CNCs. This enhancement is attributed to the anodic polymerization of surface-bound MoS_4^{2-} ligands, following the reaction:[26]

$$[MoS_4]^{2-} \rightarrow MoS_{3-x} + 1/8S_8 + 2e^-$$

Sulfur-rich MoS_x phases (*e.g.*, MoS_{3-x}) generated through anodic polymerization provide a higher density of catalytically active sites compared to amorphous MoS_x produced solely by thermal decomposition.[27,28] When a larger quantity of MoS_4^{2-} ligands remains on the CNC surface, these ligands readily undergo polymerization to form an amorphous MoS_x matrix, which can subsequently transition into the conductive 1T/1T′ phase during post-annealing. Conversely, a lower surface concentration of MoS_4^{2-} limits polymerization under identical annealing conditions, resulting in reduced 1T/1T′ phase content. The remaining amorphous domains are capable of undergoing anodic polymerization during PEC operation, leading to notable activation behavior with cycling. As shown in Fig. S10,† the *J–V* curves before and after anodic activation clearly demonstrate this effect: the photocurrent density increased by nearly tenfold following activation, thereby confirming our hypothesis. However, the stability and electrical conductivity of sulfur-rich MoS_x phases differs notably from that of the 1T/1T′ phase. To verify this effect, PEC performance was evaluated as a function of the amorphous-to-crystalline phase ratio.

The ratio of amorphous to crystalline phases in the MoS_x shell was modulated by optimizing the annealing conditions. In the case of CdSe CNCs, annealing at 500 °C, resulting in an enhanced photocurrent compared to samples treated at 300 °C. It suggests that effective phase transition of the MoS_x shell into a crystalline structure requires annealing at 500 °C. However, $CISe_2$ CNCs, which possess a lower defect formation energy,[29] are more susceptible to degradation at elevated temperatures. To address this challenge, a two-step annealing process was employed for $CISe_2$ CNCs: an initial step at 250 °C followed by a rapid thermal treatment at 500 °C to induce re-crystallization

while minimizing thermal damage to the core material. Therefore, PEC performance was subsequently evaluated under different post-annealing conditions, with the conventional 250 °C treatment denoted as the T_1 condition and the two-step process referred to as the T_2 condition. As shown in Fig. 3c, the maximum Δj value for CIS_2@MoS_x CNCs synthesized *via* the water-based method was significantly lower than that of $CISe_2$@MoS_x CNCs prepared *via* the hot injection method under both T_1 and T_2 conditions. This performance discrepancy is primarily attributed to the higher density of exposed surface defects in the water-based samples. CIS_2@MoS_x CNCs synthesized *via* the water-based method and subjected to T_2 annealing—characterized by high-temperature treatment—exhibited rapid degradation within only two operational cycles. This observation further supports the conclusion that the water-based synthesis route generates a higher density of surface defects compared to the hot-injection method.

In contrast to the defective CIS_2@MoS_x CNCs synthesized *via* the water-based method, $CISe_2$@MoS_x CNCs prepared using the hot-injection method exhibited a different trend. Specifically, $CISe_2$@MoS_x CNCs annealed under the T_1 condition displayed the highest maximum Δj value, although their dark current showed the greatest variation over six operating cycles. Meanwhile, $CISe_2$@MoS_x CNCs treated under the T_2 condition exhibited a comparable maximum Δj value but demonstrated a significantly smaller change in dark current, indicating superior operational stability with T_2 annealing condition. Since the electrochemical surface area (ECSA) of $CISe_2$@MoS_x CNCs under both T_1 and T_2 conditions showed no significant difference (Fig. 3d), the PEC performance can be primarily attributed to differences in the shell characteristics, rather than to variations in the number of active sites or surface area effects. X-ray photoelectron spectroscopy (XPS) was further conducted to investigate the shell characteristics of $CISe_2$@MoS_x CNCs under different post-annealing conditions. The Mo 3d core levels were analyzed for samples prepared without annealing, with T_1 annealing, and with T_2 annealing (Fig. 3e). The sample without post-annealing, which underwent self-polymerization during the film fabrication process, exhibited dominant Mo 3d peaks at 226.4 eV and 227.1 eV, corresponding to MoS_4^{2-} species, and at 229.2 eV and 232.6 eV, attributed to amorphous MoS_x (Fig. 3f). In contrast, the T_1- and T_2-annealed samples showed a marked decrease in the amorphous MoS_x component and the emergence of features characteristic of the 1T/1T′ phase of MoS_2 (Fig. 3g and h). Mo 3d peaks to 230.1 eV and 233.3 eV, compared to 229.9 eV and 233.3 eV for the T_1-treated sample, indicating a higher proportion of the 1T/1T′ phase. These results suggest that the higher annealing temperature in the T_2 treatment facilitates enhanced crystallization and phase transformation within the MoS_x shell.[30] Moreover, the shift in Cu 2p binding energies observed in XPS analysis provides insight into the electronic behavior, such as n-type or p-type character. Compared to the sample without post-annealing, both T_1- and T_2-annealed samples exhibited Cu 2p peaks shifted toward lower binding energies, indicating a p-type doping effect induced by the shell (Fig. S11a†). Specifically, the peaks shifted by approximately ~0.2 eV for T_1 and T_2 treatment (Fig. S11b†). These shifts suggest minor changes in the electronic band structure, likely influenced by differences in shell characteristics. However, the amorphous-to-crystalline ratio of the shell plays a crucial role in surface defect passivation—an essential factor for enhancing operational stability—while also maintaining sufficient electrical conductivity to enable effective charge transport.

Since the band structure of the MoS_x shell was not significantly affected by its amorphous-to-crystalline phase ratio, the post-annealing condition was fixed to the T_2 treatment. Subsequently, the band structure of the core material was modulated to achieve the desired reverse type-I core–shell configuration. Then, PEC performance of this reverse type-I structure was then systematically compared to that of the type II core–shell counterpart. The PEC performance of CIS_2@MoS_x CNCs with different In/Cu ratios (*i.e.*, 1.25 and 3) was evaluated, as shown in Fig. 4a and b. As the In/Cu ratio increased, the dark current density decreased from -6.4 mA cm^{-2} at -0.2 V *vs.* RHE for CIS_2@MoS_x CNCs with an In/Cu ratio of 1.25 to -1.14 mA cm^{-2} for those with a ratio of 3. On the other hand, the maximum Δj increased with the In/Cu ratio—from approximately 0.62 mA cm^{-2} for the 1.25 ratio to about 4.8 mA cm^{-2} for the 3.0 ratio—indicating enhanced charge separation efficiency. CV analyses were conducted on bare CIS_2 CNCs with In/Cu ratios of 3.0 and 1.25 to evaluate the electronic band structure of the core material in the absence of MoS_x shell. The results revealed that, for CIS_2 CNCs with an In/Cu ratio of 1.25, the CBM and VBM were located at -0.31 V and +1.18 V, respectively (Fig. 4c, d and S12a†). In contrast, for CNCs with an In/Cu ratio of 3.0, the CBM and VBM were positioned at -0.36 V and +1.06 V, respectively. As the In/Cu ratio increased, the CBM of the core material exhibited an upward shift toward that of the MoS_x shell, indicating a transition in band alignment from a type-II configuration (observed in CIS_2@MoS_x CNCs with an In/Cu ratio of 1.25) to a reverse type-I core–shell configuration (observed in those with an In/Cu ratio of 3.0). This transition to a reverse type-I band alignment is attributed to the enhanced PEC performance observed in CIS_2@MoS_x CNCs with a higher In/Cu ratio compared to those with a lower ratio. A schematic illustration of the photocathode incorporating Cu_2O/CuO/reverse type-I core–shell CNCs and their corresponding band alignment is presented in Fig. 4e. The reverse type-I core–shell configuration is characterized by a p-type core and an n-type shell. This specific band alignment not only enhances photocarrier separation under 1 sun illumination but also significantly suppresses the dark current.

When a negative potential is applied to the n-type semiconductor, the space-charge region is narrowed, resulting in a diminished degree of band bending. Under dark conditions, the core–shell junction forms a Schottky barrier that inhibits simultaneous carrier transport, thereby minimizing the dark current. Upon illumination, however, the photogenerated carriers induce a negative built-in potential, further reducing the space-charge layer and facilitating ohmic contact between the core and shell. This energy-level alignment leads to complete delocalization of electrons and holes within the shell region, promoting efficient charge separation and,

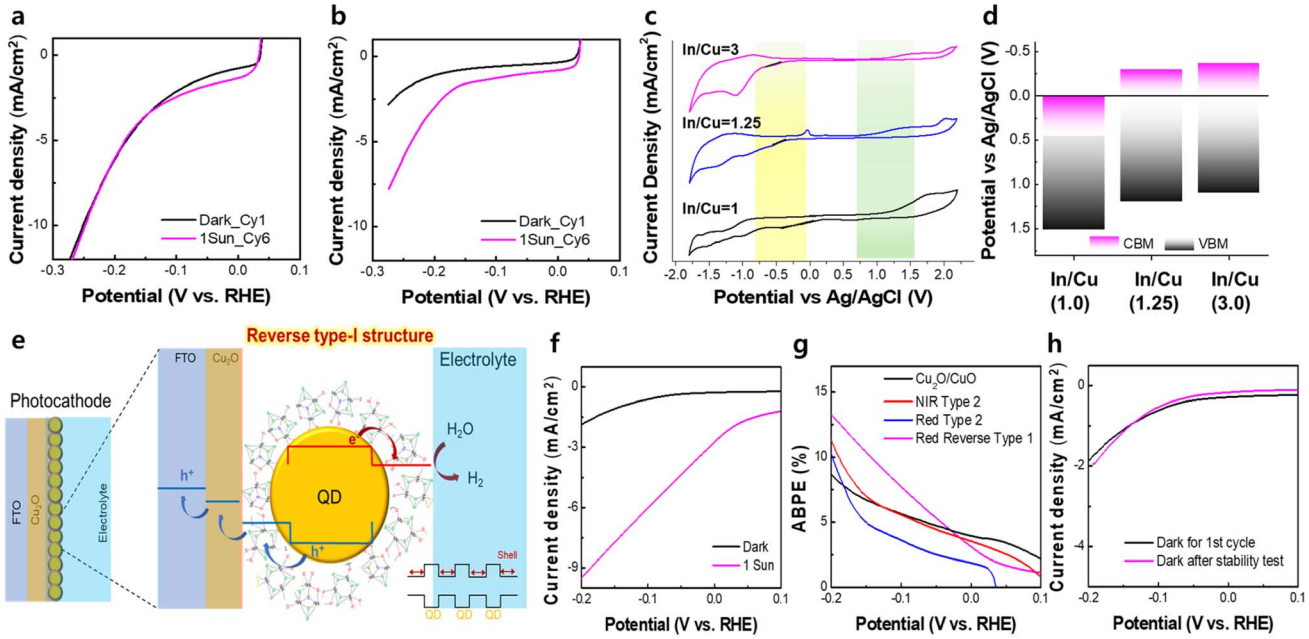

Fig. 4 (a and b) J–V curves of $CIS_2@MoS_x$ CNCs photocathodes with different In/Cu ratios: (a) 1.25 and (b) 3. (c) Cyclic voltammograms (CVs) of NIR $CIS_2@MoS_x$ CNCs with In/Cu ratios of 1.0 (black), 1.25 (blue), and 3.0 (pink) measured in 0.1 M $TBAPF_6$/acetonitrile. (d) Estimated oxidation (V_{ox}) and reduction (V_{red}) peak positions for the corresponding samples. (e) Schematic illustration of the Cu_2O/CuO/reverse type-I core–shell CNC photocathode architecture. (f) J–V curves of red $CIS_2@MoS_x$ CNC photocathodes (Cu_2O/CuO/CNC layer) with an In/Cu ratio of 3.0. (g) Applied bias photon-to-current efficiency (ABPE) plots for various types of photocathodes. (h) Dark current stability of red $CIS_2@MoS_x$ CNC photocathodes (Cu_2O/CuO/CNC layer) with an In/Cu ratio of 3.0, before and after 24 hours of continuous operation at −0.1 V *vs.* RHE.

consequently, an enhanced photocurrent density in reverse type-I core–shell CNCs. Moreover, due to the improved photocarrier separation, the operational stability at elevated working voltages is significantly enhanced in $CIS_2@MoS_x$ CNCs with an In/Cu ratio of 3.0, which exhibit the reverse type-I band alignment (Fig. S12b†). The red $CIS_2@MoS_x$ CNCs with an In/Cu ratio of 1.25 also exhibited a higher maximum Δj compared to the NIR $CIS_2@MoS_x$ CNCs with the same In/Cu ratio (Fig. S12c†). This enhancement further highlights the impact of the reverse type-I core–shell band alignment intrinsic to the red $CIS_2@MoS_x$ CNCs, a feature that is absent in their NIR counterparts. For a similar reason, the dark current densities of the red $CIS_2@MoS_x$ CNCs were markedly reduced relative to those of the NIR $CIS_2@MoS_x$ CNCs with the same composition. Ultimately, a precisely engineered reverse type-I core–shell band alignment was achieved in red $CIS_2@MoS_x$ CNCs with an In/Cu ratio of 3.0. This configuration delivered the highest photocurrent density (−9.52 mA cm^{-2} at −0.2 V *vs.* RHE) and the greatest maximum Δj among all tested samples (Fig. 4f).

Furthermore, to evaluate the photoinduced charge separation efficiency as a function of band alignment, the applied bias photon-to-current efficiency (ABPE) under standard 1 sun illumination and the incident photon-to-current efficiency (IPCE) under monochromatic illumination at 365 nm (100 mW cm^{-2}) and 650 nm (200 mW cm^{-2}) were evaluated. The ABPE in Fig. 4g of the photoelectrode passivated with reverse type I CIX_2 core–shell CNCs reached a maximum value of 13% at −0.2 V *vs.* RHE and exhibited significantly enhanced performance in the potential range below 0 V *vs.* RHE compared to both the unmodified Cu_2O/CuO electrode and the NIR/red type II CIX_2 core–shell CNCs-passivated photoelectrodes. The IPCE measurements in Fig. S13a† displayed a consistent trend: the reverse type I core–shell CNCs showed markedly higher IPCE values under both 365 nm and 650 nm illumination compared to the type II core–shell CNCs variants. This enhancement is primarily attributed to the improved light absorption characteristics of the reverse type I configuration. While the bare Cu_2O/CuO electrode demonstrates strong absorption in the 350–450 nm region, CNC-passivated films—especially those incorporating reverse type I core–shell structures—showed a significant increase in absorption above 450 nm (Fig. S13b†). This extended spectral response indicates more efficient utilization of the solar spectrum and enhanced charge transfer dynamics, likely resulting from improved electronic coupling at the core–shell interface and favorable band alignment. As a result, the reverse type I core–shell CNCs passivated photoelectrode achieved an IPCE of approximately 42% under 365 nm illumination, surpassing the performance of both the unmodified Cu_2O/CuO electrode and the type II-passivated structures. Finally, the operational stability of the reverse type I core–shell CNC photoelectrode was thoroughly investigated. Its PEC performance remained consistent, showing no significant alterations after 24 hours of operation under a constant bias of −0.1 V *versus* RHE. This outcome demonstrates a significantly improved operational stability (Fig. 4h and S13c†). To further assess the durability, electrochemical impedance spectroscopy (EIS) and CV measurements were performed after 1000 LSV cycles (0.1 V to −0.2 V *vs.* RHE). The EIS results showed no

noticeable increase in internal resistance, confirming both structural and electrochemical robustness of the photocathode (Fig. S13d†). Moreover, in contrast to the bare Cu_2O/CuO electrode, which displayed a pronounced Cu reduction peak near −0.5 V, the reverse type I core–shell CNC photocathodes exhibited no such peak (Fig. S13e†). The effective suppression of Cu reduction also contributes to the enhanced operational stability of the PEC system.

In conclusion, this study presents a universal and scalable strategy for designing narrow-bandgap shells in core–shell CNCs to enhance their performance as PEC photocathodes. The method involves ligand exchange using metal complexes, followed by a controlled annealing process, which results in the formation of a matrix-type shell composed of both amorphous and crystalline MoS_x phases. This mixed-phase structure effectively relieves interfacial lattice strain, enabling compatibility with a wide range of core materials. Importantly, despite the inherent limitations of narrow-bandgap shells—particularly their lower passivation efficiency compared to wide-bandgap materials—the matrix-type MoS_x shell significantly improves both optical and electrochemical stability. Systematic PEC performance evaluation across various ligand systems confirmed that this shell configuration provides effective surface defect passivation and enhanced charge carrier separation. Consequently, CNCs with matrix-type MoS_x shells achieved a marked increase in photocurrent generation, characterized by a high photocurrent-to-dark current ratio and excellent long-term operational stability. Further energy band alignment engineering of the core and shell facilitated the formation of reverse type-I heterojunctions in both CdSe and $CISe_2$ CNC systems. Among the configurations tested, the Cu_2O/CuO/red $CISe_2$ CNCs with a high indium content—featuring optimized band alignment and superior surface passivation—achieved the highest photocurrent density along with excellent operational stability. These findings underscore the strong potential of the matrix-type reverse type-I core–shell architecture for advancing the development of efficient and durable PEC photocathode materials.

Data availability

The data supporting this article have been included as part of the ESI.†

Author contributions

The manuscript was written through contributions of all authors. M. Kim: conceptualization, formal analysis, writing – original draft, and editing, J. M. Yeon: formal analysis and editing, G. Park and H. Kim: material synthesis and film fabrication, M. Kim and S. Y. Cho: material characteristic, S. W. Hwang and S. H. Lim: editing, resources, and supervision, H. Lee: conceptualization, editing, resources, and supervision. All authors have given their approval to the final version of the manuscript.

Conflicts of interest

There are no conflicts to declare.

Acknowledgements

This work was supported by the National Research Foundation of Korea (NRF) grant funded by the Korea government (MSIT) (no. RS-2022-00166251) and by the Ministry of Education (NRF-2022R1A6A3A01086704). This research was supported by the SungKyunKwan University and the BK21 FOUR (Graduate School Innovation) funded by the Ministry of Education (MOE, Korea) and National Research Foundation of Korea (NRF).

References

1 A. Vilanova, P. Dias, T. Lopes and A. Mendes, *Chem. Soc. Rev.*, 2024, **53**, 2388–2434.
2 H. Kim, A. Choe, S. B. Ha, G. M. Narejo, S. W. Koo, J. S. Han, W. Chung, J.-Y. Kim, J. Yang and S.-I. In, *ChemSusChem*, 2023, **16**, e202201925.
3 H. C. Lee, J. H. Park, S.-I. In and J. Yang, *Nanoscale*, 2024, **16**, 9295–9310.
4 F. Nan, S. Chen, S. Wang, Y. Lin, B. Fan, H. Li and L. Zhou, *RSC Adv.*, 2025, **15**, 9627–9635.
5 T. Tanaka, R. Tsutsumi, T. Yoshinaga, T. Sonoyama, K. Saito, Q. Guo and S. Ikeda, *RSC Adv.*, 2023, **13**, 575–580.
6 B. Liu, X.-B. Li, Y.-J. Gao, Z.-J. Li, Q.-Y. Meng, C.-H. Tung and L.-Z. Wu, *Energy Environ. Sci.*, 2015, **8**, 1443–1449.
7 C. Lu, A. Drichel, J. Chen, F. Enders, A. Rokicińska, P. Kuśtrowski, R. Dronskowski, K. Boldt and A. Slabon, *Nanoscale*, 2021, **13**, 869–877.
8 J. Cheng, L. Wu and J. Luo, *Nat. Commun.*, 2023, **14**, 7228.
9 R. A. N. Utama, R. Nabila, T. Nurtono, W. Widiyastuti, T. N. Pratiwi, I. W. Lenggoro and H. Setyawan, *Langmuir*, 2024, **40**, 27635–27644.
10 R. Vogel, P. Hoyer and H. Weller, *J. Phys. Chem.*, 1994, **98**, 3183–3188.
11 R. Wang, X. Tong, A. I. Channa, Q. Zeng, J. Sun, C. Liu, X. Li, J. Xu, F. Lin, G. S. Selopal, F. Rosei, Y. Zhang, J. Wu, H. Zhao, A. Vomiero, X. Sun and Z. M. Wang, *J. Mater. Chem. A*, 2020, **8**, 10736–10741.
12 L. Jin, H. Zhao, Z. M. Wang and F. Rosei, *Adv. Energy Mater.*, 2021, **11**, 2003233.
13 L. A. Swafford, L. A. Weigand, M. J. Bowers, J. R. McBride, J. L. Rapaport, T. L. Watt, S. K. Dixit, L. C. Feldman and S. J. Rosenthal, *J. Am. Chem. Soc.*, 2006, **128**, 12299–12306.
14 H. Kim, Y. Jeong, W.-G. Jung, M. Kim, J. Yang, M. Kim, Y. Han, H. Ko, S. W. Hwang, M. J. Kim, J. W. Lee, W.-J. Moon and H. Lee, *RSC Adv.*, 2025, **15**, 6531–6540.
15 E. Mustafa, E. A. Dawi, Z. H. Ibupoto, A. M. M. Ibrahim, A. Elsukova, X. Liu, A. Tahira, R. E. Adam, M. Willander and O. Nur, *RSC Adv.*, 2023, **13**, 11297–11310.
16 G. Liu, F. Zheng, J. Li, G. Zeng, Y. Ye, D. M. Larson, J. Yano, E. J. Crumlin, J. W. Ager, L.-w. Wang and F. M. Toma, *Nat. Energy*, 2021, **6**, 1124–1132.

17 Y. Liu, A. Xu, J. Wang, F. Jiang, H. Pang, J. Yang and Y. Zhou, *ACS Nano*, 2024, **18**, 33197–33209.
18 Y. Li, Q. Yan, J. Zhu, Y. Ren, Q. Liu, Y. Hou, J. Lu, X. Gao, X. Zhan and Q. Zhang, *ACS Sustain. Chem. Eng.*, 2023, **11**, 1019–1026.
19 L. Sygellou, *Appl. Surf. Sci.*, 2019, **476**, 1079–1085.
20 H. Lee, S. Bak, Y. Cho, M. Kim, S. H. Kang, V. Q. Bui, H. M. Le, S. W. Kim and H. Lee, *NPG Asia Mater.*, 2018, **10**, 441–454.
21 N. Elgrishi, K. J. Rountree, B. D. McCarthy, E. S. Rountree, T. T. Eisenhart and J. L. Dempsey, *J. Chem. Educ.*, 2018, **95**, 197–206.
22 C. M. Cardona, W. Li, A. E. Kaifer, D. Stockdale and G. C. Bazan, *Adv. Mater.*, 2011, **23**, 2367–2371.
23 M. Mrad, T. Ben Chaabane, H. Rinnert, B. Lavinia, J. Jasniewski, G. Medjahdi and R. Schneider, *Inorg. Chem.*, 2020, **59**, 6220–6231.
24 Z. Wu, J. Franco, B. Truijen, P. Roussel, B. Kaczer, D. Linten and G. Groeseneken, *IEEE Trans. Electron Devices*, 2021, **68**, 3246–3253.
25 H. Zhong, Z. Wang, E. Bovero, Z. Lu, F. C. J. M. van Veggel and G. D. Scholes, *J. Phys. Chem. C*, 2011, **115**, 12396–12402.
26 H. Vrubel and X. Hu, *ACS Catal.*, 2013, **3**, 2002–2011.
27 Y. Zhang, F. Gao, D. Wang, Z. Li, X. Wang, C. Wang, K. Zhang and Y. Du, *Coord. Chem. Rev.*, 2023, **475**, 214916.
28 S. S. Chougule, B. Arumugam, J. K. Alagarasan, I. Hasan, N. Thomas, V. Rajashekar, R. Srinivasan, A. K. Yadav, P. Somu, M. Lee and A. A. Jeffery, *ACS Appl. Energy Mater.*, 2024, **7**, 1949–1960.
29 S.-H. Wei and S. B. Zhang, *J. Phys. Chem. Solids*, 2005, **66**, 1994–1999.
30 O. Mabayoje, B. R. Wygant, M. Wang, Y. Liu and C. B. Mullins, *ACS Appl. Energy Mater.*, 2018, **1**, 4453–4458.